Journal of Marine Research, 53, 341–369, 1995

Photochemistry, mixing and diurnal cycles in the upper ocean

by Scott C. Doney[1], Raymond G. Najjar[2] and Scott Stewart[3]

ABSTRACT

The interplay between ocean photochemistry and surface boundary-layer physics is explored in a range of analytical and numerical process models. For simple systems, key attributes of the photochemical distribution—diurnal cycle, surface concentration, and the bulk concentration difference across the "mixed layer"—can be expressed in terms of a small number of physical (vertical diffusivity) and photochemical (turnover timescale and production depth scale) scaling factors. A coupled, 1-D photochemical/physical model is used to examine the more general case with finite mixing rates, variable photochemical production and evolving boundary layer depth. Finite boundary layer mixing rates act to increase both the diurnal cycle and mean concentration at the surface. The diurnal cycle and mean surface concentration are further amplified by coupling between photochemistry and diurnal physics. The daily heating/cooling cycle of the upper ocean can lead to a significant reduction in mixing and boundary-layer depth during the day when photochemical production is at a maximum. Accounting for these effects results in additional surface trapping of photochemically produced species and significant enhancements of the surface diurnal cycle and daily mean. The implications of our model results for field data interpretation and global air-sea flux calculations are also discussed.

1. Introduction

Photochemical reactions in seawater produce a rich variety of chemical species with turnover times ranging from μs to several days or longer (e.g. Zafiriou, 1983; Zafiriou *et al.,* 1984), similar to the physical timescales of mixing and transport in the ocean surface boundary layer. The distributions of photochemically derived species, therefore, provide a unique set of probes for short time-scale vertical advection (Johnson *et al.,* 1989) and turbulent mixing in the boundary layer and may be useful in the validation of boundary layer parameterizations (Kantha and Clayson, 1994). In a complementary fashion, the temporal and spatial patterns of photochemical

1. Climate and Global Dynamics, National Center for Atmospheric Research, Boulder, Colorado, 80307, U.S.A.
2. Department of Meteorology, Pennsylvania State University, University Park, Pennsylvania, 16802, U.S.A.
3. Department of Aerospace Engineering Sciences, University of Colorado, Boulder, Colorado, 80309, U.S.A.

species cannot be understood independent of physical mixing and dilution (Plane *et al.,* 1987; Najjar *et al.,* 1995). This is particularly true for the daily cycle, which can be strongly modified by the formation of shallow, diurnal thermoclines (Plane *et al.,* 1987; Sikorski and Zika, 1993b). Using analytical solutions and a 1-D numerical model, we examine the interaction between diurnal physics and the daily cycle and vertical profile of an idealized photochemical species over a range of conditions.

Our interest is primarily on species such as CO, COS and H_2O_2 that respond to solar and physical forcing on the hourly to several day time-scale. The concentrations of these compounds are typically elevated in the surface layer, in the case of CO and COS often supersaturated relative to the atmosphere by a factor of 10 or more, and decrease sharply with depth (Conrad *et al.,* 1982; Ferek and Andrea, 1984; Jones, 1991; Mihalopoulos *et al.,* 1992). The peak surface concentrations generally occur in the mid-afternoon, and the mean surface levels are proportional to the surface light intensity (Conrad *et al.,* 1982; Andreae and Ferek, 1992). The pronounced diurnal cycle suggest rapid chemical or biological removal mechanisms, with residence times on the order of a day or less (Conrad *et al.,* 1982; Andreae and Ferek, 1992). A correlation between surface concentration and wind speed has also been noted, which may be due to gas exchange (Conrad *et al.,* 1982) or may reflect greater mixing rates and dilution of the surface values at higher wind speeds (Najjar *et al.,* 1995; Gnanadesikan, 1995).

Turbulent mixing influences photochemical distributions by reducing surface concentrations, increasing subsurface levels, and resupplying surface water with fresh, unbleached chromophores (Plane *et al.,* 1987). The net effect depends upon both the mixing rate and vertical extent of the surface mixed layer. The surface boundary layer depth h varies with wind and buoyancy forcing, showing a distinct pattern over the day with solar heating (Fig. 1) (e.g. Price *et al.,* 1986; Woods and Barkmann, 1986; Brainerd and Gregg, 1993). The surface heat balance is normally negative (net cooling) at night due to latent, longwave and sensible heat loss, and h and mixing rates are at their maximum. Warming by the absorption of solar radiation during the day causes the water column to stratify and the region of turbulent mixing to weaken and collapse toward the surface. The formation of a diurnal thermocline leads to the shallow trapping of heat and momentum over a characteristic depth h_t, with maximum sea surface temperature (SST) anomalies normally found 2 to 4 hours following local noon (Price *et al.,* 1986). The diurnal surface temperature and velocity excesses are subsequently eroded as the boundary layer depth and mixing increase in the afternoon and evening. During periods of low wind speed and strong net heating, the trapping depth can be quite shallow, on the order of a few meters, and the diurnal variation of SST can approach 2–3°C (Stramma *et al.,* 1986; Price *et al.,* 1986; 1987).

Similar to heat, photochemically produced species will be trapped in the near-surface layer during the day. Photochemistry is, by its very nature, in phase with the

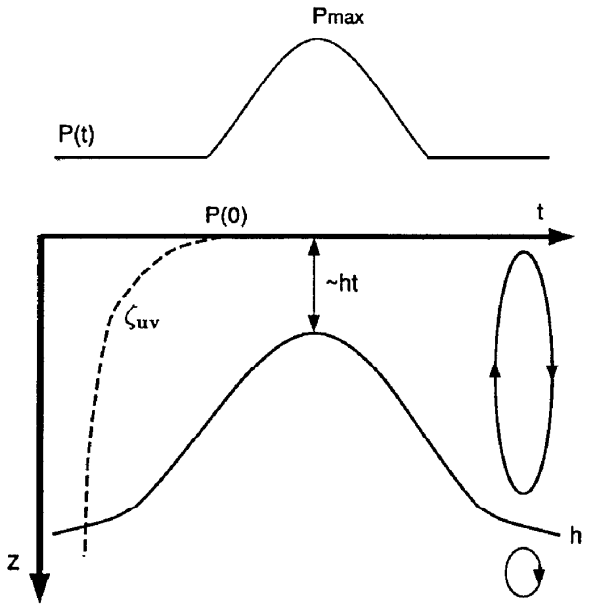

Figure 1. Schematic of diurnal cycle of photochemical production $P(t)$ and boundary layer depth h. Mixing in the boundary layer is nonlocal, dominated by large eddies with lengthscale similar to h; interior mixing is a local process. The exponential photochemical production profile $P(z) = P_0 e^{z/\zeta_{uv}}$ and photochemical trapping depth h_t are also shown.

diurnal variations of surface mixing and h (Fig. 1), and the combination of high production rates and weak mixing during the middle of the day act to enhance the amplitude of the daily surface concentration cycle (Plane *et al.*, 1987). The impact of diurnal physics on the observed photochemical signal is not well characterized, however. A major goal of this study is to identify, based on numerical model results, the behavior of the coupled photochemical/physical system over a range of physical forcing (e.g. wind stress, heating, boundary layer depth) and photochemical parameters (e.g. turnover rate, depth scale of production) and to relate this response to those of other quantities such as SST.

As a result of recent analytical and technical advances, the stage has been set for near real-time, regional surveys for a variety of transient, photochemical species (e.g. Zika *et al.*, 1993). The concepts developed here should help to distill the fundamental relationships between photochemistry and boundary layer physics from this greatly expanded data base. The role of modeling in data interpretation is especially important for underway systems, where data are collected from only a single depth and where the diurnal signal is aliased onto the spatial record. Process models can also guide the analysis of more complex, coupled physical-optical-photochemical simulations (e.g. Sikorski and Zika, 1993a, b) and identify the appropriate class of physical models to apply to specific problems.

Many of the photochemically produced compounds in the ocean play an important role in either tropospheric (e.g. CO, non-methane hydrocarbons) or stratospheric (e.g. COS) chemistry, and numerous model estimates of the global ocean source for these compounds have been proposed (Erickson, 1989; Andreae and Ferek, 1992; Erickson and Taylor, 1992; Mihalopoulos *et al.,* 1992; Plass-Dülmer *et al.,* 1993). As we will show, air-sea flux calculations are sensitive to diurnal effects as they modify the mean surface concentration seen by the atmosphere, yet many studies neglect the impact of diurnal physics. Another concern related to air-sea fluxes arises from the fact that many estimates are based on subsurface concentration measurements. Under periods of weak mixing, strong concentration gradients may develop over the upper few meters of the water column, and subsurface measurements from say an underway sampling system can underestimate the true surface concentration (Plass-Dülmer *et al.,* 1993).

Numerical modeling typically follows one of two courses: either simulation studies, where the purpose is to create a realistic model whose output is then quantitatively compared to a specific data set, or process studies, where the realism is partially sacrificed to create a cleanly posed problem where the underlying mechanisms and dynamics can be identified and better understood. The first approach requires good physical and chemical forcing data (e.g. wind stress, insolation, photochemical production and chemical loss rates) in addition to the transport model and geochemical data set. The validation of any coupled model is a difficult task, compounded in the case of ocean photochemistry by the general lack of complete data sets and relatively poor constraints for many of the relevant chemical and photochemical parameters (Appendix), and it is often difficult to separate the effects of errors in the forcing and parameter data from shortfalls in the model, even for a physical model alone (e.g. Large *et al.,* 1994). As an example, recent work by Kettle (1994) has great difficulty simulating the diurnal cycle of CO near Bermuda over a nine day period, despite the use of high temporal resolution physical forcing, a detailed spectral model of CO production, and laboratory measurements of CO removal rates (W. Martin, 1995; per. comm.). The H_2O_2 model of Sikorski and Zika (1993b) has better success but still shows large deviations from the data for about 30% of their cases.

We have chosen instead to pursue a decidedly more process-oriented approach, focusing on the role of diurnal transport on photochemical species distributions. The diurnal cycle of turbulent mixing in the upper ocean is relatively well characterized by both observations (e.g. Brainerd and Gregg, 1993) and models (e.g. Large *et al.,* 1994), and the diurnal response of our physical model has been validated against field data (Large *et al.,* 1994) and preliminary results from three-dimensional, large eddy simulations (LES). Idealized forcing and simplified photochemistry are used to highlight the physical dynamic coupling. A secondary goal is to provide a framework for interpreting existing data sets and to motivate the future collection of more photochemical data sets amenable to the simulation mode of modeling.

Table 1. Glossary of commonly used terms.

Term	Meaning	Units
C	photochemical concentration	mol m^{-3}
D	length of daylight	s
K	eddy diffusivity	$m^2 s^{-1}$
L	Monin-Obukhov length	m
P	photochemical production	mol $m^{-3} s^{-1}$
$\int Q_{net}$	total net diurnal heating	MJ m^{-2}
SST	sea surface temperature	°C
h	boundary layer depth	m
h_t	trapping depth	m
t	time	s
w_x	turbulent velocity scale	m s^{-1}
$\overline{wc}$	turbulent flux of C	mol $m^{-2} s^{-1}$
z	vertical coordinate	m
ΔC	diurnal concentration difference	mol m^{-3}
$\delta_{3,5}$	near-surface concentration difference	
λ	first-order removal rate	s^{-1}
τ	wind stress	N m^{-2}
ζ_k	eddy consumption depth	m
ζ_{uv}	photochemical production depth scale	m

Analytical solutions and scaling arguments for simple steady-state and time-varying photochemical systems are presented in Section 2. These are followed by a set of idealized, numerical experiments focusing on the coupling of photochemical production and diurnal physics (Section 3). The physical/photochemical numerical model is described in the Appendix. The emphasis in both the analytical and numerical work is to examine the factors governing the amplitude of the diurnal cycle and air-sea exchange rate and, secondarily, to lay the groundwork for future global calculations. The relevance of the model results to field data analysis and global ocean source models is discussed in Section 4.

2. Analytical solutions and scaling

For a generalized photochemical species C, the time tendency term can be described in one dimension by:

$$\frac{\partial C}{\partial t} = -\frac{\partial}{\partial z}(\overline{wc}) + \text{Production} - \text{Sink} \tag{1}$$

where z and $\overline{wc}$ are the vertical coordinate and turbulent flux of C (Table 1); both are defined as positive in the upward direction. The solution of Eq. 1 requires the photochemical production and chemical/biological sink rates as a function of time and depth. Photolysis of dissolved organic matter in seawater by ultraviolet UV radiation (280–350 nm) serves as the source for many of the species of interest (e.g.

CO, COS, H_2O_2) (Conrad *et al.*, 1982; Ferek and Andreae, 1984). The sinks are more various and species specific and may involve microbial uptake (e.g. CO; Conrad *et al.*, 1982), chemical reactions (e.g. COS by inorganic hydrolysis; Andreae and Ferek, 1992) and/or possibly particle mediated removal (e.g. H_2O_2; Sikorski and Zika, 1993b). The approach followed here is to use a simple model for both photochemical production and chemical loss, with the understanding that more detailed simulations could be constructed for any particular species (e.g. Sikorski and Zika, 1993a, b).

Photochemical production rates depend on a variety of factors including the intensity and spectral character of the subsurface irradiance field, the amount and absorption spectra of photoactive chromophores, and the quantum yield of the reaction in question (e.g. Plane *et al.*, 1987; Sikorski and Zika, 1993a). The equations controlling the photochemical production rate can be simplified greatly if it is assumed that: (i) the concentration of chromophore is uniform and fixed with time; (ii) the reaction is mediated by irradiance from a single wavelength of light; and (iii) the attenuation lengthscale ζ_{uv} for that wavelength is also uniform with depth and time. The rationale behind these assumptions is discussed in more detail in the Appendix. The production term in Eq. 1 then is given by:

$$P(z, t) = P_0(t)e^{z/\zeta_{uv}} \tag{2}$$

where the surface production $P_0(t)$ (mol m^{-3} s^{-1}) is proportional to the UV irradiance at the surface. The total production over the water column is proportional to the surface production and UV attenuation scale, $\int_{-\infty}^{0} P(z, t)dz = P_0(t)\zeta_{uv}$. At a similar level of sophistication, the sink term for C is treated simply as a first-order process with a uniform loss constant λ (s^{-1}). Finally, the turbulent flux term $\overline{wc}$ is replaced, following the classical analogy with molecular diffusion, by $-K\partial C/\partial z$ where K (m^2 s^{-1}) is an eddy diffusivity. Eq. 1 then reduces to:

$$\frac{\partial C}{\partial t} = \frac{\partial}{\partial z} K \frac{\partial C}{\partial z} + P_0(t)e^{z/\zeta_{uv}} - \lambda C. \tag{3}$$

a. Mixing and vertical profiles: K and C(z). Insight into the behavior of Eq. 3 can be gained from analytical solutions to special cases. Consider the case with uniform production and no mixing:

$$P_0 e^{z/\zeta_{uv}} = \lambda C,$$

which has the steady state solution:

$$C(z) = \frac{P_0}{\lambda} e^{z/\zeta_{uv}}. \tag{4}$$

Any arbitrary profile will approach this profile with an e-folding time governed by the turnover time, λ^{-1}.

Mixing tends to reduce the surface concentration and near surface gradient relative to the no-mixing limit. The simplest case is that with uniform mixing and small ζ_{uv} such that the production term can be treated as a surface boundary condition:

$$K\frac{d^2C}{dz^2} = \lambda C,$$

with $dC/dz|_0 = P_0\zeta_{uv}/K$ and $dC/dz|_{-\infty} = 0$, whose solution is:

$$C(z) = \frac{P_0}{\lambda}\frac{\zeta_{uv}}{\zeta_k}e^{z/\zeta_k}. \tag{5}$$

The concentration decreases exponentially with depth with a scale equal to the "eddy consumption depth" ζ_k (e.g. Johnson, 1981):

$$\zeta_k = \left(\frac{K}{\lambda}\right)^{1/2}. \tag{6}$$

The surface concentration C_0 varies linearly with ζ_k^{-1}. For a mean value of $K = 100\ \mathrm{cm^2\ s^{-1}}$ and $\lambda^{-1} = 5$ hr (an average for COS; Najjar *et al.*, 1995), the eddy consumption depth ζ_k is 13.5 m. To what depth, then, can C be considered "well-mixed"? If this depth is taken as the depth at which the concentration is 90% of the surface value, the "well-mixed" region extends to approximately $0.1\zeta_k$, or only 1.3 m.

Uniform mixing and depth varying production can be combined, still in steady-state:

$$K\frac{d^2C}{dz^2} + P_0e^{z/\zeta_{uv}} = \lambda C.$$

The solution for this equation with boundary conditions $dC/dz|_0 = 0$, and $dC/dz|_{-\infty} = 0$ is:

$$C(z) = \frac{P_0}{\lambda}\frac{\zeta_{uv}^2}{\zeta_{uv}^2 - \zeta_k^2}\left(e^{z/\zeta_{uv}} - \frac{\zeta_k}{\zeta_{uv}}e^{z/\zeta_k}\right). \tag{7}$$

The profile $C(z)$ now varies with both ζ_{uv} and ζ_k and reduces Eq. 5 as $\zeta_{uv} \to 0$. The normalized surface concentration is a nonlinear function of the two depth scales, $C_0\lambda/P_0 = \zeta_{uv}/(\zeta_{uv} + \zeta_k)$. The dependence on the production scale ζ_{uv} arises because the initial profile is more uniform for larger ζ_{uv}, and thus mixing is less effective at lowering C_0 by dilution.

In the real ocean, the region of surface mixing does not extend infinitely (Fig. 1). This can be accounted for by changing the lower boundary conditions for the

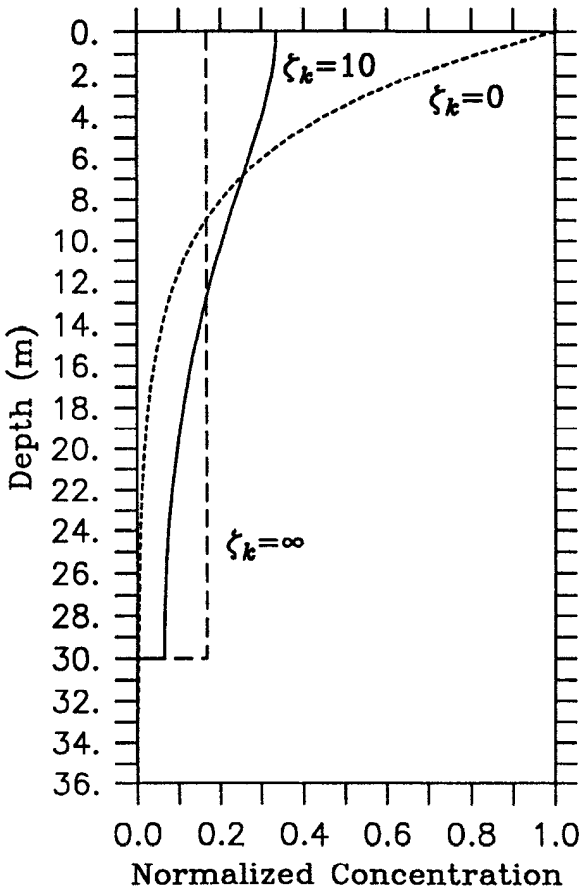

Figure 2. Steady-state analytical solutions of normalized concentration $C(z)$ for fixed surface photochemical production and a mixed layer depth $h = -30$ m. Three cases are shown: no-mixing ($\zeta = 0$) (. . .), moderate mixing ($\zeta = 10$ m) (—), and infinite mixing ($\zeta = \infty$) (- -).

differential equations to $dC/dz|_h = 0$, where h is the "mixed-layer" depth ($K = 0$ for $z < -h$). For the general case with photochemical production, this leads to:

$$C(z) = \frac{P_0}{\lambda}\frac{\zeta_{uv}^2}{\zeta_{uv}^2 - \zeta_k^2}\left[e^{z/\zeta_{uv}} - \frac{\zeta_k}{\zeta_{uv}}e^{z/\zeta_k} - \frac{\zeta_k}{\zeta_{uv}}\frac{\cosh(z/\zeta_k)}{\sinh(-h/\zeta_k)}(e^{-h/\zeta_{uv}} - e^{-h/\zeta_k})\right] \qquad (8)$$

$$-h < z < 0.$$

Vertical profiles computed from Eq. 8 are shown in Figure 2 for three cases: no mixing ($\zeta_k = 0$), moderate mixing ($\zeta_k = 10$ m) and infinite mixing ($\zeta_k = \infty$). Relative to the no-mixing case, the effect of mixing is to deplete the near surface region with a corresponding enhancement deeper in the water column. The depth where the two profiles intersect marks the transition point where the diffusive tendency term is zero; above that depth diffusion acts as a sink for C while below it serves as a source.

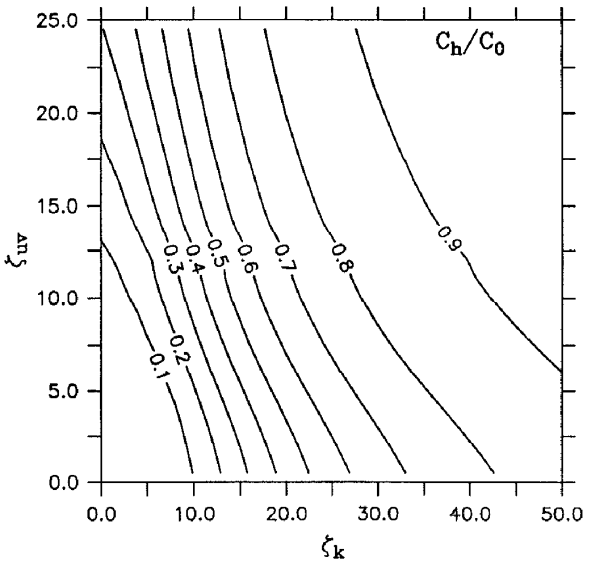

Figure 3. Concentration ratio between the base of the "mixed layer" and the surface, C_h/C_0, as a function of the eddy-consumption length ζ_k and photochemical production scale ζ_{uv}. The mixed layer depth is $h = -30$ m.

The two extremes of no-mixing and infinite mixing over a mixed layer depth h provide upper and lower bounds for surface concentration C_0.

The concentration for the moderate mixing case differs by about a factor of four from the surface to the base of the mixed layer in Figure 2, denoting the finite time for material to be mixed over h. The ratio C_h/C_0 is a useful diagnostic for the extent to which the "mixed-layer" is actually well mixed. The C_h/C_0 ratio from Eq. 8 has been solved for numerically as a function of ζ_k and ζ_{uv}, shown in Figure 3. When ζ_k is small relative to h, the tracer is mixed over only a fraction of the boundary layer before removal and the concentration at the mixed layer base is small compared with that at the surface. When ζ_k is comparable to or larger than h, the mixed layer is almost homogeneous in C. The C_h/C_0 ratio also shows a weak sensitivity to ζ_{uv}, reflecting the relative vertical asymmetry and surface intensification of the photochemical production (Fig. 1). Increasing or decreasing h causes the "well-mixed" region in Figure 3, C_h/C_0 near 1, to contract or enlarge, respectively.

b. Time-varying production: P(t). A different family of solutions to Eq. 3 arise with time varying production, $P(t)$. Neglecting mixing and depth dependence (or alternatively solving for concentration over a homogeneously mixed layer driven by a mean production value) leads to:

$$\frac{dC}{dt} = P(t) - \lambda C.$$

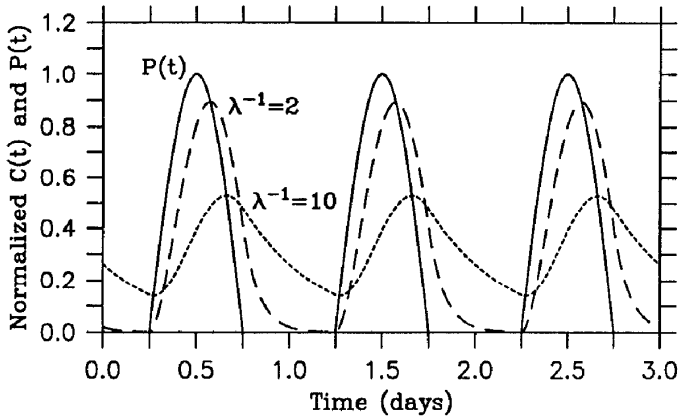

Figure 4. Analytical solutions (Eq. 10) of concentration versus time for an idealized diurnal photochemical production cycle $P(t)$ (—) (Eq. 9). The length of daylight D = 12 hours. Daily $C(t)$ cycles are shown for turnover times of λ^{-1} = 2 hours (- -) and λ^{-1} = 10 hours (- -), and the $C(t)$ curves are normalized by P_{max}/λ.

A reasonable approximation to a daily cycle is given by a half sinusoid during the day and zero at night (Fig. 4):

$$P(t) = P_{max} \sin \frac{\pi t}{D} \qquad 0 \le t < D$$
$$P(t) = 0 \qquad D \le t < T \tag{9}$$

where D is the length of daylight, T is 24 hours, and the time t has been shifted for convenience so that sunrise occurs at $t = 0$. The stable solution over several repeating days is then:

$$C(t) = \frac{P_{max}}{\lambda}\left(\frac{1}{1+\frac{\pi^2}{D^2\lambda^2}}\right)\left[\sin\left(\frac{\pi t}{D}\right) - \frac{\pi}{D\lambda}\cos\left(\frac{\pi t}{D}\right)\right.$$
$$\left. + \frac{\pi}{D\lambda}\left(\frac{1+e^{-\lambda(T-D)}}{1-e^{-\lambda T}}\right)e^{-\lambda t}\right] \qquad 0 \le t < D \tag{10}$$
$$C(t) = \frac{P_{max}}{\lambda}\frac{\pi}{D\lambda}\left(\frac{1}{1+\frac{\pi^2}{D^2\lambda^2}}\right)\left(\frac{1+e^{\lambda D}}{1-e^{-\lambda T}}\right)e^{-\lambda t} \qquad D \le t < T.$$

Typical solutions to Eq. 10 are shown in Figure 4 for D = 12 hours and turnover times of λ^{-1} = 2 hours and λ^{-1} = 10 hours.

Similar to observations, the peak concentration C_{max} occurs several hours after the maximum production rate. The time lag is nearly proportional to λ^{-1} at rapid

turnover rates, leveling off to a maximum of about 4 hours as the turnover time approaches the daylength. The size of the peak concentration also decreases, in a normalized sense, with λ^{-1}. This is related to the response time, given by λ^{-1}. For slower response times, the concentration is further from the steady-state value P/λ at any particular time and the diurnal cycle is dampened. Increasing daylength D in Eq. 10 reduces the diurnal cycle and increases the peak time lag.

The diurnal cycle can be characterized in several ways, and we choose to utilize the fractional signal $\Delta C/\overline{C}$, where ΔC is the peak to trough difference and $\overline{C}$ is the daily mean. A significant diurnal cycle, taken as a 15% variation $\Delta C/\overline{C} = 0.3$, is found for turnover time less than about 36 hours. The presence or absence of a daily cycle, defined in this manner, is governed only by the turnover time, not by the absolute production rate (Conrad *et al.,* 1982; Jones, 1991); increasing the production rate results in larger concentrations but does not change the fractional daily signal.

c. Coupling between photochemistry and diurnal physics: h(t) and P(t). The diurnal cycle also can be affected by variations in the boundary depth $h(t)$ (Plane *et al.,* 1987). For a fixed inventory, changing h alters the depth over which the tracer is spread in the vertical and leads to a daily cycle in C_0 even if production is constant with time. Since $P(t)$ and $h(t)$ are generally in phase (i.e. shallow h during the middle of the day when photochemical production is near its maximum; Fig. 1), the sense of the coupling with the diurnal physics is to enhance the peak concentration and size of the diurnal cycle relative to the case with fixed h.

The interaction between the photochemical and physical diurnal cycles can be roughly characterized by a photochemical trapping depth, which we define from scaling arguments as:

$$h_t = \frac{\int_t \int_z P_{\text{net}}}{\Delta C_0}. \tag{11}$$

The trapping death h_t reflects the change in surface concentration ΔC_0 normalized by the net production, $P_{\text{net}} = P - \lambda C$, integrated over depth and time from the point in the morning when the net production turns positive to the maximum surface value. A small value of h_t implies weak mixing during the day, surface trapping and a strong diurnal photochemical response. Conversely, a deeper h_t marks stronger mixing and a weaker, damped daily signal for the same total input. The photochemical trapping depth is similar in general concept to the trapping depth for heat presented by Price *et al.* (1986).

The photochemical trapping depth h_t will depend on several parameters: the evolution of the boundary layer depth h and diffusivity profile $K(z)$ over the day and the attenuation depth ζ_{uv}. The response of h to wind and buoyancy forcing were

mentioned in the introduction, the daily minimum h varying from essentially zero (no wind and large insolation) to the mixed layer depth defined by the stratification of the seasonal thermocline (high wind and low isolation). The eddy diffusivity also scales with the surface fluxes via a turbulent velocity scale w_x and is proportional to the boundary layer depth in our formulation (see Appendix and Large *et al.*, 1994). As mixing tends toward zero, we expect the maximum diurnal signal and h_t to approach a minimum equal to the production depth ζ_{uv}. The maximum trapping depth depends upon the depth of the night-time convective layer $h_{\max}$ set by the seasonal stratification. The sensitivity to diurnal physics, therefore, will be greater for tracers with smaller ζ_{uv}. Since much of the solar heating is due to infrared radiation that is absorbed in the upper few ten's of centimeters (see Eq. 18), the photochemical and thermal responses should diverge at very low wind speeds.

The complexity of the analytical solutions incorporating time histories for $h(t)$ and $P(t)$ becomes rapidly daunting, in part because one must account for the entrainment/detrainment of C from the mixed layer as well as the photochemical production in the diurnal thermocline. At this stage, therefore, we progress to a full numerical model.

3. Numerical model results

The mechanics of the coupled, photochemical/physical model used in the following numerical experiments are presented in the Appendix. Model cases are run with fixed wind stress and surface heat loss and a daily varying solar heating rate, and solutions are shown at approximate steady-state after several days of spin-up. The model boundary layer depths h are constrained by a strong thermocline at 28 meters, and salinity profiles are uniform with $S = 35\ ^0/_{00}$.

The physical model results for temperature and scalar diffusivity are shown in Figure 5 for a typical diurnal cycle. During the night, surface cooling and convection result in a nearly well mixed boundary layer, with a small (0.05°C) unstable surface layer (Fig. 5a) (Anis and Moum, 1992; Large *et al.*, 1994). Solar heating leads to rapid shoaling of the boundary layer and the formation of a diurnal thermocline and jet (not shown). Following sunset, surface cooling erodes the stratification, deepens the boundary layer h, and redistributes momentum and tracers vertically. The diurnal variation in SST is about 0.25°C, with the maximum value lagging the solar forcing by 2.5 hours. Diffusivities (Fig. 5b) are large during the night-time, peak values exceeding 300 $cm^2\ s^{-1}$. Daytime diffusivities are more than an order of magnitude lower due to the smaller h and reduction in the turbulent velocity scale w_x under stable forcing. Note that a substantial level of interior mixing occurs in the diurnal thermocline below the boundary layer throughout the day and early evening.

The steady-state solutions for an idealized photochemical species C ($\zeta_{uv} = 5$ m, $\lambda^{-1} = 12$ hours) are shown in Figure 6 with the standard full diurnal physics and with wind-driven mixing only. For the wind mixing only case, the surface heat loss and

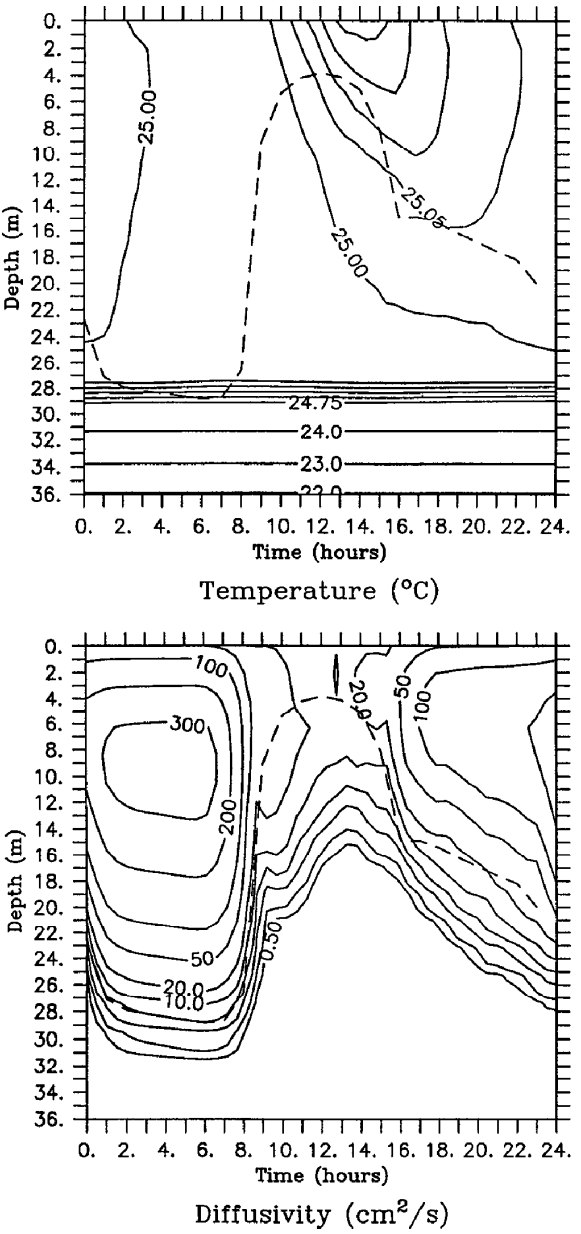

Figure 5. Numerical model solution for daily cycles of (a) potential temperature Θ (°C) and (b) scalar diffusivity K_s ($cm^2\ s^{-1}$) versus time and depth for standard case (30N, year day 83, $Q_{ns} = -215\ W\ m^{-2}$, $\tau_x = 0.05\ N\ m^{-2}$ or about 6 m s^{-1}). The boundary layer is constrained by a strong thermocline at 28 meters, and the diurnal cycle of the PBL depth h is shown by the dashed line (- -). The model solutions are shown at approximate steady-state after several days of spin-up.

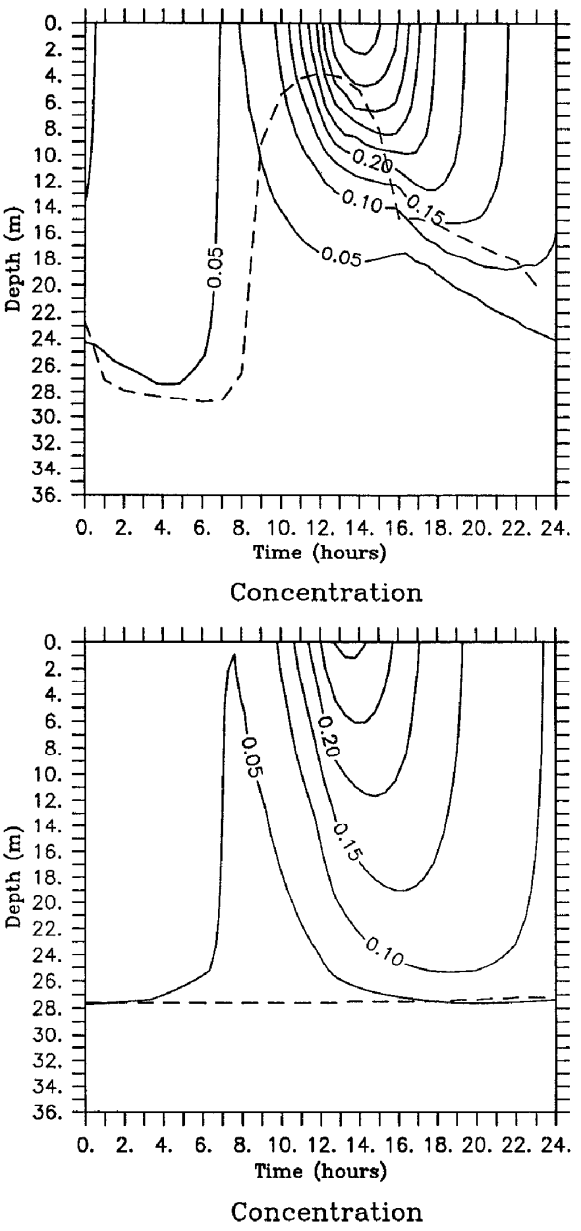

Figure 6. The steady-state solutions for an idealized photochemical species C (ζ_{uv} = 5 m, λ^{-1} = 12.0 hr) versus time and depth for two cases: (a) full diurnal physics and (b) neutral, wind-driven mixing only. The diurnal cycle of the PBL depth h is shown by the dashed line (- -). Concentrations are normalized to the maximum surface concentration found if there were no mixing.

solar heating terms are set to zero, and the diffusivity profiles are simply the neutral forms of Eq. 15 with uniform h and wind stress (Najjar *et al*, 1995). In both cases, a strong surface maximum develops over the day with peak concentrations a few hours after noon. This surface excess is then redistributed in the vertical by turbulent mixing, and by early morning, the remaining amount of C is spread nearly uniformly over the boundary layer depth. The turbulent flux $\overline{wc}$ in the full physics case (Fig. 7a) is downward (negative) everywhere and is largest near dusk when the diffusivities are increasing but substantial vertical gradients from the day still remain. The turbulent flux divergence $d\overline{wc}/dz$ field (Fig. 7b) reflects the overall effect of mixing on the concentration distribution, with generally negative values (net sink) in the upper 5 meters and positive values (net source) below that depth. A ridge of strong positive values tracks the afternoon deepening of h and is associated with the arrival of the daily maximum at subsurface depths. This behavior differs from that in the wind mixing only case, where the time lag at depth is controlled primarily by the turbulent mixing timescale (Najjar *et al.*, 1995).

As expected, the standard solution with full diurnal physics shows a significantly stronger diurnal signal than the wind mixing only case, with elevated surface concentrations, stronger near surface gradients and lower concentrations at depth during the day (Fig. 6). Key differences in the diurnal response for the two cases are characterized in Table 2. Values are also given in Table 2 for the two extremes, no mixing and infinite mixing to the maximum nighttime boundary layer depth. The peak $C_0^{\max}$ and daily mean $\overline{C}_0$ surface values for the standard case are enhanced, compared to the wind mixing only case, by 57% and 39%, respectively. The stronger diurnal cycle is also apparent in the photochemical trapping depth, which decreases from 14.2 m to 8.5 m as diurnal physics is added. Both cases contain noticeable near surface concentration gradients during the middle of the day (Fig. 6), which are diagnosed in the model solutions as the fractional concentration difference from the surface grid point (0.5 m) to a depth of 3.5 m, chosen to approximate the intake depth for underway systems:

$$\delta_{3.5} = (C_0 - C_{3.5})/C_0. \tag{12}$$

This concentration difference reaches a maximum of about 13% during the day for the standard solution and is still evident in the afternoon and evening because of the finite boundary layer mixing rates in the model.

The sensitivity of the coupled model to variations in wind stress and total net heat input has been explored and is presented in Figure 8. The wind stress is constant for each simulation, and is varied from zero to 0.2 N m^{-2}, or about a wind speed of 12.5 m s^{-1}. The total net heat input $\int Q_{\text{net}}$ (MJ m^{-2}), defined as the integral of the total net heating over the period when solar radiation exceeds surface heat loss, is adjusted by multiplying the daily solar input function by a constant. The wind mixing only solution shown in Figure 6b is equivalent to the special case where $\int Q_{\text{net}} = 0$.

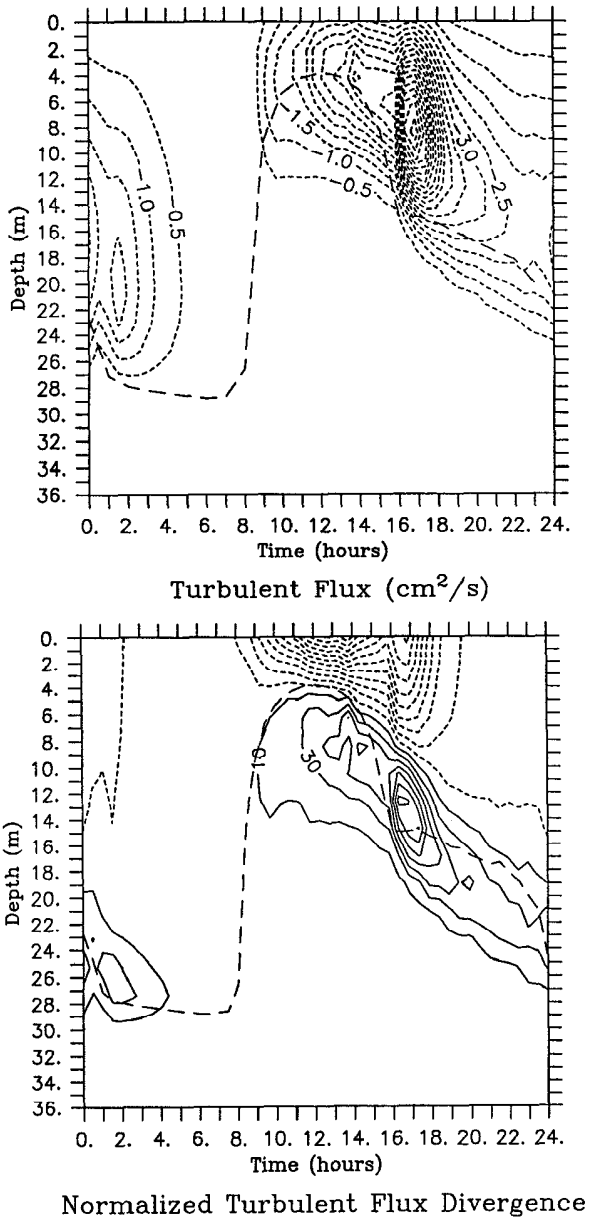

Figure 7. Contour plots of (a) normalized turbulent tracer flux $\overline{wc}$ (cm s^{-1}) and b) turbulent flux divergence $d\overline{wc}/dz$ (day^{-1}) versus time and depth for the standard, full physics solution shown in Figure 6. The diurnal cycle of the PBL depth h is shown by the dashed line (- -).

Table 2. Comparison of the diurnal cycle of an idealized photochemical species for various levels of physics. Values are given for the mean $\overline{C_0}$ and maximum C_0^{max} surface concentrations, the concentration difference between the maximum and minimum surface values ΔC_0, the photochemical trapping depth h_t, and $\delta_{3.5} = (C_0 - C_{3.5})/C_0$. All concentrations are normalized by the maximum surface concentration for the case with no mixing.

	$\overline{C_0}$	C_0^{max}	ΔC_0	h_t	$\delta_{3.5}$
no mixing	0.59	1.00	0.73	5.0	50.4%
full physics	0.19	0.48	0.43	8.5	13.3%
wind mixing only	0.14	0.31	0.26	14.0	12.9%
infinite mixing	0.10	0.17	0.13	28.9	—

At low wind speeds and moderate $\int Q_{net}$, the model response is dominated by wind stress, and the mean surface concentration $\overline{C_0}$ and trapping depth h_t approach the values found for the no mixing limit (Table 2). As wind speed increases, the amplitudes of the mean concentration and diurnal cycle both decrease. The change in the trapping depth is stronger than that in the surface mean, leading to a reduced fractional diurnal signal at large τ. The solutions also show a dependence on the total heat input $\int Q_{net}$ that becomes more pronounced at low $\int Q_{net}$. The addition of a diurnal heating/cooling cycle produces stronger mixing at night, due to the surface heat loss driven convection, and weaker mixing during the day (Figs. 5 and 6). This is reflected in the enhanced diurnal cycle, lower h_t, and slightly larger surface mean value at higher $\int Q_{net}$ relative to the wind mixing only limit ($\int Q_{net} = 0$). The near surface profile, approximated by $\delta_{3.5}$ varies sharply at low wind speeds, reaching values of greater than 40%.

4. Discussion and summary

The analytical work in Section 2 suggests that the general behavior of the coupled photochemical/physical system in the upper ocean can be expressed with a small set of scaling parameters (ζ_k, ζ_{uv}, λ^{-1}) related to properties of the specific tracer and to the overall boundary layer (see also Gnanadesikan, 1995 for another discussion on scaling). Several broad conclusions can be drawn. First, the presence of a significant fractional diurnal cycle depends primarily on the turnover time λ^{-1} and will occur for species with turnover times less than a few days. Second, the mixing timescale for the ocean boundary layer is finite, and significant vertical gradients in photochemical tracers will persist even in the "mixed-layer," the degree of which can be expressed roughly with the eddy consumption depth $\zeta_k = (K/\lambda)^{1/2}$. Physical and chemical characteristics need to be considered when choosing the appropriate physical model for a particular problem. Models that predict boundary layer diffusivities (e.g. *K*-profile, Large *et al.,* 1994; or second-order closure, Kantha and Clayson, 1994) may be required for tracers with short residence times (e.g. CO, COS) while less complex,

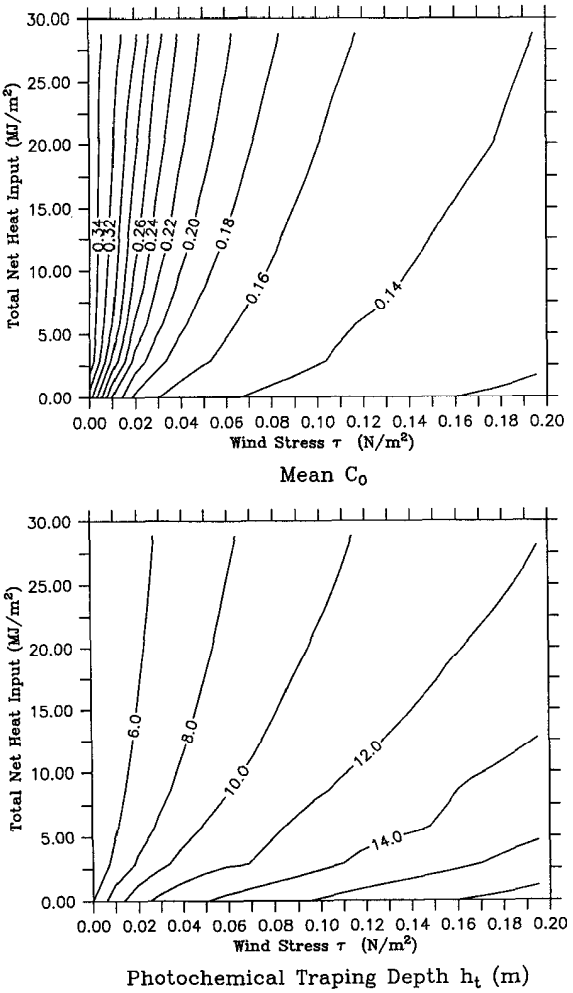

Figure 8. Sensitivity of coupled physical/photochemical model behavior to wind stress τ (N m^{-2}) and total net heat input $\int Q_{net}$ (MJ m^{-2}), defined as the integral of the total net heating over the period when solar radiation exceeds surface heat loss. Contour plots are shown for (a) mean daily surface concentration $\overline{C_0}$, (b) photochemical trapping depth h_t and (c) near surface concentration difference $\delta_{3.5}$. The mean concentration has been normalized to the maximum surface value in the case of no mixing.

bulk mixed layer models (e.g. Price *et al.*, 1986) may suffice for more slowly responding tracers such as H_2O_2 that have fairly uniform concentrations over the mixed layer (Sikorski and Zika, 1993b). Third, tracers with a shallow production depth scale ζ_{uv} are more sensitive to mixing, particularly at low wind speed. For practical purposes, this suggests that it will be difficult to develop proxy measures, such as daily SST variations, for photochemical tracers.

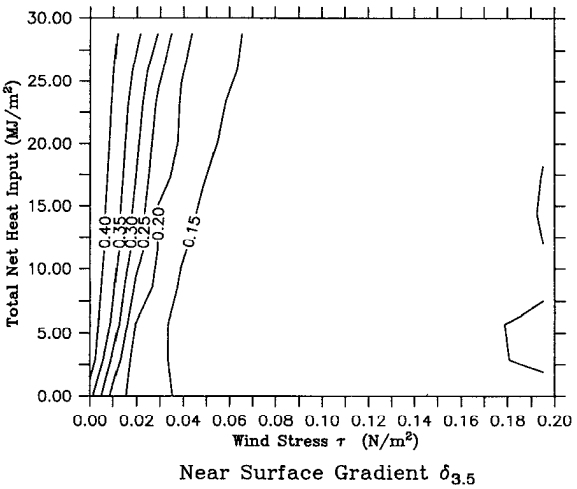

Figure 8. (Continued)

The numerical model solutions in Section 3 are used to examine the more general circumstance of finite mixing rates, variable photochemical production, and evolving boundary layer depth. Turbulent mixing serves to redistribute photochemical tracers in the vertical, acting as a surface sink and subsurface source. The finite boundary layer mixing rate introduces an additional mixing timescale, h^2/K, which amplifies the fractional diurnal signal at the surface (compare, for example, $\Delta C_0/\overline{C}_0$ for the four cases in Table 2). The finite mixing timescale hinders the transport of tracer away from the surface and thus reduces the effective dilution of C_0 during the day. In contrast at night, there is no production to compete against mixing, the vertical tracer gradient is reduced nearly to zero, and the minimum surface concentration approaches the limit of a well mixed boundary layer (Fig. 6). The finite mixing time also leads to larger peak concentration differences across the boundary layer (C_h/C_0) than in the steady solutions (Fig. 3).

The numerical results highlight the importance of coupling between photochemistry and boundary layer physics on the diurnal timescale. The daily cycle of surface heating and cooling leads to a shoaling of the surface boundary layer and reduction in the turbulent mixing rates during the day. The resulting effect on photochemical tracer distributions is to strengthen the surface diurnal signal and elevate the mean surface concentration $\overline{C}_0$. The photochemical trapping depth h_t is developed as a measure of the diurnal photochemical response, reflecting the depth scale over which the incremental net production is spread. Variations of a factor of 2–3 in $\overline{C}_0$ and h_t were found over a typical range of wind stress and net heating. The effect of including diurnal heating and cooling at a fixed wind stress was less dramatic but still lead to changes in h_t and $\overline{C}_0$ on the order of 50% for our standard case.

The general features of the numerical results can be compared in a qualitative

fashion with available photochemical data sets (a more quantitative test would require high resolution observations and forcing data and an elaborate optical/photochemical model; Sikorski and Zika, 1993a). The normalized amplitude ($C_{max}/C_{min} = 10$) and phase lag (2–2½ hours) of the diurnal cycle in the standard model case (Fig. 6) are within the range of typical reported values for CO (Swinnerton *et al.*, 1970; Conrad *et al.*, 1982) and COS (Ferek and Andreae, 1984; Andreae and Ferek, 1992). In contrast with the model, Conrad *et al.* (1982) downplay the role of turbulent mixing on the surface concentration and show no time lag between surface and subsurface maximum concentrations. The model subsurface maxima are broad in time (Fig. 6), however, and the conclusions of Conrad *et al.* (1982) are based on rather coarse space and time resolution data.

The model also predicts sharp, near surface concentration gradients over the middle of the day, broadly consistent with observations. Conrad *et al.* (1982), for example, observed CO concentrations from the surface to 1 meter to be a factor of two higher than those at 4 meters depth, and Plass-Dülmer *et al.* (1993) found surface alkane concentrations exceeding those at 11 meters by up to a factor of five at low wind speeds. Though the model-predicted surface gradients are somewhat suspect due to sensitivity to vertical resolution and missing physics, they nevertheless suggest that corrections may be necessary for underway systems under low wind speed conditions. The size of the average daily bias resulting from the near-surface gradient ($\sim$10–35%; Table 2 and Fig. 8c) is small relative to our present, overall uncertainty in the air-sea fluxes but may become more relevant as future efforts attempt to refine these estimates.

The results of our numerical model have implications for global and regional models of the air-sea fluxes of photochemically-produced species. Previous studies have estimated global air-sea fluxes of COS and CO by determining simple relationships between these chemical species and other proxy data, such as surface chlorophyll and surface solar radiation (Erickson, 1989; Andrae and Ferek, 1992; Erickson and Eaton, 1993). Najjar *et al.* (1995) suggest extending this approach by developing a simple mixed layer model which includes seasonal and spatial variations in mixed-layer turbulence, using climatological surface winds and mixed layer depths. Here, we introduce the importance of resolving the diurnal cycle in mixed layer physical processes, since we find that ignoring this diurnal cycle can substantially underestimate the mean surface concentration of a photochemically-produced species, particularly at low wind speeds. Since the effect of diurnal physics is greatest at low wind speeds and since the air-sea gas transfer velocity increases with increasing wind speed, the effect of diurnal physics may have less importance for global, as opposed to regional, trace gas budgets.

The general phenomena of diurnal trapping due to reduced boundary layer mixing during the day is relevant to a variety of other systems. For example, the growth rates

for nutrient-replete phytoplankton populations can be on the order of 2–3 doublings per day, suggesting that phytoplankton populations will show similar vertical gradients and diurnal oscillations to those discussed here. Of course the diurnal signal for phytoplankton may be partially masked by the additional complexity of the background phytoplankton profile, governed by light limitation and inhibition, nutrient limitation and zooplankton grazing. The timescales for some photoadaptation processes are also in the range responsive to diurnal physical coupling (Prézelin *et al.,* 1991). In general, any property that undergoes short time-scale fluctuations can couple with diurnal physics, potentially leading to nonlinear effects.

The numerical model solutions in Section 3 are directed primarily at subtropical and tropical, open ocean environments. In more productive, coastal waters, which form a disproportionate fraction of the ocean source for some photochemical species (e.g. COS, Andreae and Ferek, 1992), both the scales of diurnal trapping and photochemical production will be reduced. In polar regions, the diurnal thermocline will be much weaker because the density structure is controlled more by salinity than temperature since the thermal expansion coefficient is smaller at low temperature. Seasonal variations may also be important as the vertical amplitude of the diurnal boundary layer migration may be largest in the spring when the seasonal mixed layer is still deep and there is significant net heating during the day (Woods and Barkmann, 1986).

As with all numerical simulations, the photochemical/physical model presented here can only capture the behavior of processes that are explicitly included. Fully resolving near-surface property gradients, for example, may require more detailed treatment of short-wave absorption (Kantha and Clayson, 1994) and the parameterization of the physical effects of Langmuir cells (Weller and Price, 1988) and wave mixing, evident as enhanced surface dissipation (Shay and Gregg, 1986; Brainerd and Gregg, 1993). Further improvements may also arise from progress on the parameterization of nonlocal and asymmetric boundary layer transport under convective conditions (Wyngaard, 1987), while at the other extreme, questions also remain regarding boundary layer physics under strongly stabilizing conditions (see Appendix). Finally, additional coupling behavior may arise in simulations of field data with more realistic transient wind and buoyancy forcing.

Acknowledgments. We wish to thank W. Large and J. McWilliams for their insight and encouragement and D. Erickson, who pointed out the importance of near-surface gradient in air-sea trace gas exchange. Two anonymous reviewers provided useful comments and suggestions regarding the manuscript. W. Holland and L. Kantha provided funding for S. Stewart during the initial phases of this project. This work was begun while both S. Doney and R. Najjar were Postdoctoral Fellowships under the Advanced Study Program at NCAR. The National Center for Atmospheric Research is sponsored by the National Science Foundation.

APPENDIX

Numerical photochemical/physical model

a. Physical model. The physics of the surface mixed layer and near surface, stratified region are simulated numerically with a nonlocal, boundary layer parameterization developed by Large *et al.* (1994). The model predicts the vertical turbulent fluxes in the oceanic planetary boundary layer (PBL) using large yet finite eddy diffusivities K_x. The magnitude of the eddy diffusivities and thus mixing vary as a function of the surface wind stress τ, surface buoyancy forcing $\overline{wb}_0$, and boundary layer depth h. The boundary layer depth h is defined as the penetration depth for surface generated turbulence and depends upon the stratification, velocity shear and surface buoyancy forcing. The time evolution for a mean property X (momentum or scalar) at any depth z in the model is given by:

$$\frac{\partial X}{\partial t} = -\frac{\partial}{\partial z}(\overline{wx}) + \text{Source/Sink.} \tag{13}$$

The turbulent flux $\overline{wx}$ and vertical coordinate z are defined as positive in the upward direction. Solar absorption and photochemical processes are included in the net source/sink term; for the velocity components U and V, this term also accounts for the Coriolis effect. A brief overview of the model is given below; for a more thorough description the reader is referred to Large *et al.* (1994).

The turbulent fluxes in the boundary layer are formulated in terms of a depth dependent diffusivity $K_x(z)$ and a nonlocal or countergradient term γ_x:

$$\overline{wx}(z) = -K_x(z)\left[\frac{\partial X}{\partial z} - \hat{\gamma}_x\right] \qquad -h < z < 0. \tag{14}$$

The shape of the PBL diffusivity profile $K_x(z)$ is specified as a function of the distance $d = -z$ from the surface, and the magnitude is determined by a turbulent velocity scale $w_x(z)$ and the depth of the boundary layer:

$$K_x(z) = hw_x\left[\frac{d}{h}\left(1 - \frac{d}{h}\right)^2\right]. \tag{15}$$

$K_x(z)$ reaches a maximum at a third of the PBL depth and tends toward zero at both the surface and h. The turbulent velocity scale w_x differs for momentum and scalars and increases with surface wind stress and unstable surface buoyancy forcing (i.e. net cooling and evaporation) (Large *et al.*, 1994). Bulk absorption of solar radiation over the PBL acts to damp surface generated turbulence by lowering w_x. For a typical wind speed of 6 m s^{-1} and a 30 m, neutral boundary layer, the peak scalar diffusivity value at $1/3h$ is about 120 cm^2 s^{-1}, leading to a PBL mixing timescale of approximately 20

hours. Nighttime convection driven by surface cooling from evaporation and longwave heat flux tends to decrease the mixing timescale considerably.

The nonlocal term γ_x stems from atmospheric observations and model results that show significant turbulent heat fluxes in convective PBLs over regions of zero mean temperature gradient, reflecting the asymmetric and non-local nature of turbulence in a convective PBL (e.g. Deardorff, 1966). In the following simulations, γ_x is nonzero only for potential temperature, Θ, and is parameterized using the turbulent surface heat flux (Large *et al.,* 1994).

The PBL depth h is determined prognosticly based on a bulk Richardson number stability criteria (Troen and Mahrt, 1986; Large *et al.,* 1994), where the bulk Richardson number Ri_b relative to the surface is defined as:

$$Ri_b(d) = \frac{(B_r - B(d))d}{|V_r - V(d)|^2 + V_t^2(d)}. \tag{16}$$

Surface reference values of buoyancy B_r and velocity V_r, taken as the average values over the upper 10% of the PBL, are used instead of the model surface values themselves to reduce the resolution dependence of the model results. The depth h is taken to be the smallest value of d at which Ri_b equals the critical value of 0.3 The extra term $V_t^2(d)$ in the denominator accounts for unresolved shear generated by surface turbulence. $V_t^2(d)$ is set to give the correct entrainment flux for the pure convective case (Large *et al.,* 1994). During periods of stable buoyancy forcing, for example mid-day with strong solar heating of the boundary layer, the boundary depth h is limited to the Monin-Obukov lengthscale L (see Turner, 1973; Large *et al.,* 1994).

The behavior of the ocean boundary layer depth under strongly stabilizing conditions is not well determined, and several different scales have been proposed for the thermal trapping depth h_t, a proxy for the mean boundary layer depth during the day. For free convection ($\tau = 0$), a convective depth can be defined from the solar radiation profile $Q_s(z)$ and net surface heat loss Q_{ns} such that the density profile is stable when the water column is uniformly mixed to that depth (Dalu and Purini, 1982). The minimum convective depth can be quite shallow under strong, noontime heating conditions (e.g., ~ 1 m) and is the relevant scale only at very low wind speeds (Price *et al.,* 1986). As wind stress increases, the trapping depth should vary with τ and inversely to Q_{net}. Price *et al.* (1986) propose $h_t \propto (\tau/Q^{1/2})(\Gamma_\tau/\Gamma_Q^{1/2})$, where the Γ's are related to the diurnal heating timescale. This form is appropriate for mixed layer parameterizations based on a mean flow Richardson number and is broadly consistent with observations (Price *et al.,* 1987). Alternative parameterizations suggest that h_t should go as the Monin-Obukov depth L during periods of strong heating and stabilization, $h_t \propto \tau^{3/2}/Q$ (Turner, 1973). Both forms predict small values of h_t, on the order of a few meters, for low wind speeds and strong heating (Price *et al.,* 1986; 1987).

The numerical model results shown in Figures 5 and 6 follow the latter, Monin-Obukhov scaling, and the boundary layer depth shoals to a minimum 3.8 m at mid-day in response to this constraint. Note that the interior mixing scheme (see below) generates significant diffusivities below the boundary layer during the day, and the boundary layer diffusivities at mid-day are partially driven from below (Kim and Mahrt, 1992; Large *et al.,* 1994). A transition in h occurs near hour 16 when buoyancy forcing switches from stable (net heating) to unstable (net cooling) and the model determination of h shifts from $h = L$ to h computed from the bulk Richardson number (Eq. 16). Following the transition, h shoals briefly because the increased mixing (Fig. 6b) reduces the shear squared term in Eq. 16 faster than the buoyancy term. Removing the Monin-Obukhov constraint altogether results in generally deeper values of h but very weak boundary layer diffusivities because of the small turbulent velocity scale at large z/L. The net effect is that the mean profiles of Θ and C are rather insensitive to the specification of h. The Large *et al.* (1994) model differs in this respect from bulk mixed layer models (e.g. Price *et al.,* 1986), where the boundary layer shoals but remains well-mixed under strongly stable forcing.

The vertical fluxes of momentum and scalars below the PBL, $z < h$, in the interior of the model are formulated in a similar fashion to the PBL scheme using eddy diffusivity profiles K_x and vertical property gradients $\partial X/\partial z$. Interior mixing resulting from resolved shear instability, found to be important for capturing the diurnal SST cycle (Large *et al.,* 1994), is parameterized using the local gradient Richardson number. The background internal wave mixing is treated via small, constant diffusivities, 1×10^{-4} m^2 s^{-1} for momentum and 1×10^{-5} m^2 s^{-1} for scalars (Gregg, 1987; Ledwell *et al.,* 1993). The diffusivity values and gradients from the interior and boundary layer schemes are matched across h by modifying Eq. 15; under some circumstances, the diffusivity in the boundary layer can be driven from below.

The physical model is forced with prescribed surface values of wind stress τ, solar Q_s and non-solar or turbulent Q_{ns} heat flux (the sum of sensible, latent and net longwave fluxes), and net freshwater flux F. The simulations in section 3 are run with constant values of τ and Q_{ns}, and $F = 0$. The turbulent heat loss term Q_{ns} is set to equal the daily integrated heating rate for solar radiation absorbed in the boundary layer, and the loss of heat out the bottom of the model due to internal wave diffusion is balanced by a surface heat flux that does not enter into the diffusivity calculations. The daily cycle of Q_s is computed from the radiation at the top of the atmosphere ($Q_s^0 = 1368$ W m^{-2}) corrected for the effects of solar zenith angle θ and atmospheric transmission. θ is equal to 0° when the sun is directly overhead and is calculated from a simple geometric model as a function time of day, year day, and latitude. Atmospheric transmission for the clear sky case is given from the okta cloud model of Dobson and Smith (1988):

$$Q_s = (1.00 - 0.07)\, Q_s^0 \cos\theta(0.400 + 0.386 \cos\theta). \tag{17}$$

The okta model was chosen over other potential cloud models because of its simplicity and because it was developed and tested against hourly rather than daily mean data. A fixed surface albedo of 7% is applied to the incoming solar radiation.

Solar radiation is allowed to penetrate below the ocean surface leading to sub-surface heating and photochemical production. The sub-surface profile of bulk solar radiation $Q_s(z)$ is specified with a two band approximation:

$$Q_s(z) = Q_s(0)[fe^{z/\zeta_{s1}} + (1 - f)e^{z/\zeta_{s2}}]. \tag{18}$$

The two bands roughly correspond to an infrared and red band that is absorbed in the upper meter and a blue-green visible band that can penetrate 10's of meters depending on the water type. The depth scales and band fraction f are taken from Paulson and Simpson (1977) for clear, open ocean water (Jerlov water type I: $f = 0.58$, $\zeta_{s1} = 0.35$, $\zeta_{s2} = 23$). The sub-surface heating rate dT/dt due to solar absorption is calculated from $dT/dt = (dQ_s/dz)/(\rho c_p)$, where ρ is density and c_p is the specific heat.

The time evolution of U, V, Θ, S, and C are computed by numerically integrating the finite-difference forms of equation 13. The model domain is 0–40 m with a 1 m resolution grid, and the lower-boundary conditions for velocity and scalars are specified constant values and open flux, determined by the gradient and interior diffusivity. The integration scheme is a semi-implicit, iterative technique with a time step Δt of 5 minutes. Further details of the numerical treatment and grid resolution issues can be found in Large *et al.* (1994).

The behavior of the physical model has been validated against oceanic observations over a range of timescales (diurnal to interannual) and environments (subtropical to subpolar North Pacific) (Large *et al.,* 1994; Large and Crawford, 1995). In general, the model appears to perform comparable or slightly better than other available one-dimensional models. In particular, it demonstrates a significant improvement in the model treatment of episodic mixing events and the exchange of properties between the surface boundary layer and seasonal thermocline.

b. Photochemical model. An outline of the photochemical/optical component model was introduced with the analytical modeling in Section 2. The model captures the essential elements of ocean photochemical cycles without including the complexity of a true simulation (e.g. Sikorski and Zika, 1993a, b). The main features of the photochemical model are: photochemical production proportional to a surface UV flux; depth dependence of production set by a single attenuation scale; and simple, first-order removal kinetics. A brief discussion on the underlying rationale for the photochemical model, the appropriate parameter ranges and the functional form of the surface UV radiation field are given below.

Ocean photochemical processes are driven primarily by the photodissociation of dissolved organic matter by UV radiation (280–350 nm). Quantitative estimates for

production rates are currently difficult to come by for many of the species of interest and even when available may vary by an order of magnitude across different ocean regions (e.g. CO; Kettle, 1994). Since our interest lies primarily in identifying processes rather than in simulating individual data sets, we choose to normalize the absolute production to the surface ultraviolet flux parameterized below.

The wavelength dependence for the photochemical production is also neglected, and the photochemical production rate thus decreases exponentially in the water column with a single scale depth, ζ_{uv}. Typically as one moves to lower, more energetic wavelengths in the *UV* the apparent quantum yield for a photochemical reaction increases while the available surface *UV* flux decreases sharply, and the competition between the two often leads to a characteristic peak in the production spectra (e.g. Kettle, 1994). Using a detailed spectral model for the photochemical production of CO, Kettle (1994), for example, showed that the majority of the production occurred between 300–340 nm and that the resulting profile of production over the day closely resembled a simple exponential with an attenuation length of about 5 meters. The attenuation length for *UV* radiation in seawater varies with wavelength and depends upon the dissolved organic matter and to a lesser degree on the chlorophyll concentration, ranging from 6.5–19 m (300–350 nm) in very clear waters to 1.0–2.1 m for the same wavelength band in productive, coastal waters (chlorophyll concentration of 5 mg m^{-3}) (Baker and Smith, 1982). The attenuation length for the global mean surface chlorophyll concentration of 0.14 mg m^{-3} (Yoder *et al.,* 1993) at 315 nm (the middle of the UV-B) is about 7 m. We set ζ_{uv} equal to 5 m in our standard case.

Ultraviolet radiation in the atmosphere decreases more rapidly with zenith angle than the total shortwave flux. Field data from Behr (1992) show for a wide latitude range over the Atlantic (40N to and 30S) that the fraction of UV-B (295 to 330 nm) to total shortwave varies primarily as a function of zenith angle, with only weak dependence on cloud cover and total ozone column. A fit of Behr's (1992) data reveals that the UV-B fraction is very nearly proportional to $\cos^2 \theta$ (Najjar *et al.,* 1995), and we model the surface production P_0 as:

$$P_0 \propto Q_s \cos^2 \theta. \tag{19}$$

where the constant of proportionality is arbitrary since only normalized results are presented.

The use of a simple, first order kinetic loss term (Eq. 3) is consistent with laboratory studies for both CO (Kettle, 1994) and COS (Elliot *et al.,* 1987). The specific turnover rates for photochemical species vary widely depending on the species and environmental conditions. For example, Conrad *et al.* (1982) observed strong diurnal cycling of CO in North Atlantic surface waters with residence times less than 3–4 hours, in sharp contrast with the much longer CO turnover times of 25 to 2922 hours and lack of a diurnal cycle found by Jones (1991) in the Sargasso Sea. An intermediate value of 52 ± 25 hours was measured for near surface water (0–75 m)

in the Sargasso Sea by Kettle (1994), who also present literature values for ocean CO turnover ranging from 4–100 hours. Elliot *et al.* (1987) report that COS residence times due to loss by hydrolysis range from 5–20 hours, depending on pH and temperature. The typical turnover times for H_2O_2 in the eastern Caribbean was measured by Moore *et al.* (1993) to be longer, 30–120 hours. The wide range of turnover rates precludes the use of any single value for λ^{-1} as representative of all photochemical species in general or even any individual species. An intermediate value for the removal time of $\lambda^{-1} = 12$ hours is chosen for our standard numerical simulation because it is within the reported range for CO or COS in the regime where substantial diurnal cycles are observed (see also Section 2b).

The simplicity of the photochemical/optical model can be criticized on several grounds, none serious enough, however, to warrant the added complexity. By using a single attenuation length ζ_{uv}, we neglect photochemical production due to visible wavelengths deeper in the water column, which may be important for H_2O_2, for example (Sikorski and Zika, 1993a). Also, the attenuation coefficient for even a single wavelength is an apparent optical property and can vary over the day because of the angular dependence on underwater pathlength for direct radiation (Sikorski and Zika, 1993a). Within the model is an implicit assumption that the supply of photochemical precursors is vertically homogeneous and constant with time; neither condition may hold, however, and additional coupling with the physical dynamics may arise from the mixing up of unbleached chromophores (Plane *et al.,* 1987). Although first-order kinetics is used to parameterize the removal mechanism, other functional forms (e.g. Michaelis-Menten kinetics; photochemical decomposition; depth dependencies) may be more appropriate for certain situations. Finally, the loss of tracer due to air-sea gas exchange is neglected in the model. This term appears to be minor in the overall photochemical budget under typical conditions (Najjar *et al.,* 1995; Gnanadesikan, 1995).

REFERENCES

Andreae, M. O. and R. J. Ferek. 1992. Photochemical production of carbonyl sulfide in seawater and its emission to the atmosphere. Global Biogeochem. Cycles, *6,* 175–183.

Anis, A. and J. N. Moum. 1992. The superadiabatic surface layer of the ocean during convection. J. Phys. Oceanogr., *22,* 1221–1227.

Baker, K. S. and R. C. Smith. 1982. Bio-optical classification and model of natural waters. 2. Limnol. Oceanogr., *27,* 500–509.

Behr, H. D. 1992. Net total and UV-B radiation at the seas surface. J. Atmosp. Chem., *15,* 299–314.

Brainerd, K. E. and M. C. Gregg. 1993. Diurnal restartification and turbulence in the oceanic surface mixed layer 1. Observations. J. Geophys. Res., *98,* 22,645–22,656.

Conrad, R., W. Seiler, G. Bunse and H. Giehl. 1982. Carbon monoxide in seawater (Atlantic Ocean). J. Geophys. Res., *87,* 8839–8852.

Dalu, G. A. and R. Purini. 1982. The diurnal thermocline due to buoyant convection. Quart. J. R. Met. Soc., *108,* 929–935.

Deardorff, J. W., 1966. The counter gradient heat flux in the lower atmosphere and in the laboratory. J. Atmos. Sci., *23,* 503–506.

Dobson, F. W. and S. D. Smith. 1988. Bulk models of solar radiation at sea. Q.J.R. Meteorol. Soc., *114,* 165–182.

Elliot, S., E. Lu and S. Rowland. 1987. Carbonyl sulfide hydrolysis as a source of hydrogen sulfide in open ocean seawater. Geophys. Res. Lett., *14,* 131–134.

Erickson, D. J. III. 1989. Ocean to atmosphere carbon monoxide flux: Global inventory and climate implications. Global Biogeochem. Cycles, *3,* 305–314.

Erickson, D. J. III and B. E. Eaton. 1993. Global biogeochemical cycling estimates with CZCS satellite data and general circulation models. Geophys. Res. Lett., *20,* 683–686.

Erickson, D. J. III and J. A. Taylor. 1992. 3-D tropospheric CO modeling: the possible influence of the ocean. Geophys. Res. Lett., *19,* 1955–1958.

Ferek, R., and M. O. Andreae. 1984. Photochemical production of carbonyl sulfide in marine surface waters. Nature, *307,* 148–150.

Gnanadesikan, A. 1995. Effects of mixed layer dynamics on the diurnal cycle of photochemically produced species: Special focus on carbon monoxide. J. Geophys. Res., (submitted).

Gregg, M. C. 1987. Diapycnal mixing in the thermocline: A review. J. Geophys. Res., *92,* 9686–9698.

Johnson, J. E. 1981. Lifetime of carbonyl sulfide in the troposphere. Geophys. Res. Lett., *8,* 938–940.

Johnson, K. S., S. W. Willason, D. A. Wiesenburg, S. E. Lohrenz and R. A. Arnone. 1989. Hydrogen peroxide in the western Meditteranean Sea: a tracer for vertical advection. Deep-Sea Res., *36,* 241–254.

Jones, R. D. 1991. Carbon monoxide and methane distribution and consumption in the photic zone of the Sargasso Sea. Deep-Sea Res., *38,* 625–635.

Kantha, L. H. and C. A. Clayson. 1994. An improved mixed layer model for geophysical applications. J. Geophys. Res., *99,* 25,235–25,266.

Kettle, A. J., 1994. A model of the temporal and spatial distribution of carbon monoxide in the mixed layer. M.S. Thesis, Massachusetts Institute of Technology and Woods Hole Oceanographic Institution, Woods Hole, MA, 215 pp.

Kim, J. and L. Mahrt. 1992. Simple formulation of turbulent mixing in the stable free atmosphere and nocturnal boundary layer. Tellus, *44A,* 381–394.

Large, W. G. and G. B. Crawford, 1995. Observations and simulations of upper ocean response to wind events during the Ocean Storms Experiment. J. Phys. Oceanogr., (in press).

Large, W. G., J. C. McWilliams and S. C. Doney, 1994. Oceanic vertical mixing: a review and a model with a nonlocal boundary layer parameterization. Rev. Geophys., *32,* 363–403.

Ledwell, J. R., A. J. Wilson and C. S. Low. 1993. Evidence for slow mixing across the pycnocline from an open-ocean tracer-release experiment. Nature, *364,* 701–703.

Mihalopoulous, N., B. C. Nguyen, J. P. Putaud and S. Belviso. 1992. The oceanic source of carbonyl sulfide (COS). Atmosp. Environ., *26A,* 1383–1394.

Moore, C. A., C. T. Farmer and R. G. Zika. 1993. Influence of the Orinoco River on hydrogen peroxide distribution and production in the Eastern Caribbean. J. Geophys. Res., *98,* 2289–2298.

Najjar, R. G., D. J. Erickson III and S. Madronich. 1995. Modeling the air-sea fluxes of gases formed from the decomposition of dissolved organic matter: carbonyl sulfide and carbon monoxide, *in* The Role of Non-living Organic Matter in the Earth's Carbon Cycle, R. Zepp and C. Sonntag, (eds.), John Wiley, New York (in press).

Paulson, C. A. and J. J. Simpson. 1977. Irradiance measurements in the upper ocean. J. Phys. Oceanogr., *7,* 952–956.

Plane, J. M. C., R. G. Zika, R. G. Zepp and L. A. Burns. 1987. Photochemical modeling applied to natural waters, *in* Photochemistry of Environmental Aquatic Systems, R. G. Zika and W. J. Cooper, eds., American Chemical Society, Washington, D.C., 250–267.

Plass-Dülmer, A. Khedim, R. Koppmann, F. J. Johnen, J. Rudolph and H. Kuosa. 1993. Emissions of light nonmethane hydrocarbons from the Atlantic into the atmosphere. Global Biogeochem. Cycles, *7,* 211–228.

Prézelin, B. B., M. M. Tilzer, O. Schofield and C. Haese. 1991. The control of the production process of phytoplankton by the physical structure of the aquatic environment with special reference to its optical properties. Aquatic Sci., *53,* 136–186.

Price, J. F., R. A. Weller, C. M. Bowers and M. G. Briscoe. 1987. Diurnal response of sea surface temperature at the long-term upper ocean study (34°N, 70°W) in the Sargasso Sea. J. Geophys. Res., *92,* 14,480–14,490.

Price, J. F., R. A. Weller and R. Pinkel. 1986. Diurnal cycling: Observations and models of the upper ocean response to diurnal heating, cooling, and wind mixing. J. Geophys. Res., *91,* 8411–8427.

Shay, T. J. and M. C. Gregg. 1986. Convectively driven turbulent mixing in the upper ocean. J. Phys. Oceanogr., *16,* 1777–1798.

Sikorski, R. J. and R. G. Zika. 1993a. Modeling mixed-layer photochemistry of H_2O_2: Optical and chemical modeling of production. J. Geophys. Res., *98,* 2315–2328.

—— 1993b. Modeling mixed-layer photochemistry of H_2O_2: Physical and chemical modeling of distribution. J. Geophys. Res., *98,* 2329–2340.

Stramma, L., P. Cornillon, R. A. Weller, J. F. Price and M. G. Briscoe. 1986. Large diurnal sea surface temperature variability: satellite and in situ measurements. J. Phys. Oceanogr., *16,* 827–837.

Swinnerton, J. W., V. J. Linnebom, and R. A. Lamontagne. 1970. The ocean: A natural source of carbon monoxide. Science, *167,* 984–986.

Troen, I. B. and L. Mahrt. 1986. A simple model of the atmospheric boundary layer; sensitivity to surface evaporation. Boundary Layer Meteorol., *37,* 129–148.

Turner, J. S. 1973. Buoyancy Effects in Fluids. Cambridge University Press, New York, 368 pp.

Weller, R. A. and J. F. Price. 1988. Langmuir circulation within the oceanic mixed layer. Deep-Sea. Res., *35,* 711–747.

Woods, J. D. and W. Barkmann. 1986. The response of the upper ocean to solar heating. I: The mixed layer. Quart. J. R. Met. Soc., *112,* 1–27.

Wyngaard, J. C. 1987. A physical mechanism for the asymmetry in top-down and bottom-up diffusion. J. Atmosp. Sci., *44,* 1083–1087.

Yoder, J. A., C. R. McClain, G. C. Feldman and W. E. Esaias. 1993. Annual cycles of phytoplankton chlorophyll concentrations in the global ocean: A satellite view. Global Biogeochem. Cycles, *7,* 181–194.

Zafiriou, O. C. 1983. Natural water photochemistry, *in* Chemical Oceanography, Academic Press, London. U.K., *8,* 339–379.

Zafiriou, O. C., J. Joussot-Dubien, R. G. Zepp and R. G. Zika. 1984. Photochemistry of natural waters. Environ. Sci. Tech., *18,* 358A–371A.

Zika, R. G., P. J. Milne and O. C. Zafiriou. 1983. Photochemical species of the eastern caribbean: an introductory overview. J. Geophys. Res., *98,* 2223–2232.

Received *15 September, 1994;* revised: *17 January, 1995.*